Available online at www.sciencedirect.com
SCIENCE DIRECT®
Journal of Computational Physics 203 (2005) 744–760
JOURNAL OF COMPUTATIONAL PHYSICS
www.elsevier.com/locate/jcp

Discretization on quadrilateral grids with improved monotonicity properties

Jan Martin Nordbotten [a,*], Geir Terje Eigestad [b]

[a] Department of Mathematics, University of Bergen, Joh. Brunsgt. 12, 5008 Bergen, Norway
[b] Center of Integrated Petroleum Research, University of Bergen, Norway

Received 22 March 2004; received in revised form 29 September 2004; accepted 1 October 2004

Abstract

Multi-point flux approximation (MPFA) discretization methods have been applied in the oil industry since the mid 1990s. The discretizations are based on a control volume formulation and the finite difference structure makes general skew grids and unstructured grids feasible in a fully implicit formulation. MPFA methods are therefore suitable for flow problems in realistic reservoirs. Monotonicity issues are known to arise for high aspect ratios combined with skewness of computational grids for MPFA methods. In this paper, we improve the MPFA discretization techniques for general quadrilateral grids, such that the above difficulties are handled to give a more robust discretization of the governing equations for fluid flow in porous media. Comparisons to the MPFA O-method are made, and the suggested discretization is shown to be an improvement in regards to monotonicity. For smooth solutions, the method performs equally well as the O-method when the convergence is examined.

Keywords: Anisotropy; Control-volume; Heterogeneous; MPFA

1. Introduction

Numerical simulation of multi-phase porous media flow in three dimensions poses great challenges. The absolute permeability tensor in the single phase flux expression $\boldsymbol{q} = \boldsymbol{K}\nabla u$ will for general anisotropic, inhomogeneous media be a full tensor with discontinuous spatial variability. In practical applications, the multi-phase flow solutions themselves may also have large spatial and temporal variability, and possibly also discontinuities in the formation of shocks.

* Corresponding author. Tel.: +47 55584869.
E-mail address: jan.nordbotten@mi.uib.no (J.M. Nordbotten).

0021-9991/$ - see front matter © 2004 Elsevier Inc. All rights reserved.
doi:10.1016/j.jcp.2004.10.002

Control-volume methods have shown themselves to be very well suited in this setting. In particular, control-volume methods allow fully implicit solution techniques of the governing equations. This allows for stable solutions without prohibitively restrictive time steps, as may be needed in sequential and IMPES (implicit pressure, explicit saturation) formulations.

The class of control-volume multi-point flux approximation (MPFAs) methods [1–13] and its conceptual equivalents [14–17] have proved themselves to be very good extensions of the one-dimensional harmonic mean, and are easily adaptable to implicit settings. The MPFA methods are defined in two dimensions for quadrilaterals [1,2,10] and general polygonals [5,6]; and in three dimensions for tetrahedra and hexahedra [4,10], or combinations of these geometric elements [17]. No constraints are imposed on the regularity of the elements, and the element faces need not match [7–9]. The methods are defined both in physical space and in transformed reference spaces. Convergence of the methods for discontinuous permeability cases are investigated numerically in [11,15]. All MPFA methods are locally mass conservative; they also reproduce uniform flow fields exactly when defined in physical space [11]. However, for very skew elements, or severe non-aligned anisotropy, the MPFA methods on quadrilaterals display some problems with monotonicity [12,13].

Alternative discretizations to MPFA methods include finite element (FE) [18–20], discontinuous Galerkin (DG) [21], control volume finite element (CVFE) [22,23], mixed finite element (MFE) [24], control volume mixed finite element (CVMFE) [25,26], hybrid mixed finite element (HMFE) [27], and expanded mixed finite element (EMFE) [28,29] methods. Although all of these methods have their strengths, in the context of multi-phase porous media flow some of them may also have drawbacks. In particular, FE lacks local mass conservation for cases with discontinuous coefficients [30]; DG, MFE and EMFE are computationally slow due to many more degrees of freedom and indefinite linear systems; CVFE does not handle discontinuous permeability satisfactory [22,31] and experiences monotonicity problems [23]; HMFE as well as MFE are better suited for sequential rather than implicit solution procedures; and CVMFE encounters problems on general hexahedral cells [26] in three dimensions. For these reasons, MPFA has been chosen for implementation in simulators such as Eclipse [32], the general purpose research simulator at Stanford [17], and research simulators at Norsk Hydro [33] and ChevronTexaco [34].

We will herein present an extension of the MPFA methodology, which is an improved method for discretizations with adverse combinations of grid skewness and aspect ratios combined with permeability anisotropy. This improves a potential weakness of current MPFA methods.

To fix ideas, we will look at the elliptic model pressure equation arising from porous media flow

$$-\int_{\Omega} \nabla \cdot (\boldsymbol{K} \nabla p)\, \mathrm{d}V = q, \tag{1}$$

which relates the pressure p to the sources and sinks q through the permeability $\boldsymbol{K}$ of the medium in a domain Ω. Under appropriate smoothness conditions and zero pressure boundary conditions, Eq. (1) has the solution [35]

$$p(\boldsymbol{x}) = \int_{\Omega} q(\boldsymbol{\xi}) G(\boldsymbol{x}, \boldsymbol{\xi})\, \mathrm{d}\boldsymbol{\xi}. \tag{2}$$

The Green's function G satisfies a maximum principle [36], which together with the zero pressure boundary condition implies

$$G(\boldsymbol{x}, \boldsymbol{\xi}) \geqslant 0. \tag{3}$$

Thus the operator $\mathscr{L}(q) = \int_{\Omega} q(\boldsymbol{\xi}) G(\boldsymbol{x}, \boldsymbol{\xi})\, \mathrm{d}\boldsymbol{\xi}$ is monotone (a linear operator $\mathscr{L}$ is monotone if either $\mathscr{L}(f) \leqslant \mathbf{0}$ or $\mathscr{L}(f) \geqslant \mathbf{0}$ for all $f \geqslant 0$). We would like this consequence of the maximum principle to carry over to the discrete formulation. The monotonicity property is also desirable for parabolic equations, as discussed in [6].

MPFA discretizations yield approximations to Eq. (1) in the form

$$\boldsymbol{M}\boldsymbol{p} = \boldsymbol{q}, \tag{4}$$

where $\boldsymbol{M}$ is a banded matrix, and $\boldsymbol{p}$ and $\boldsymbol{q}$ are vectors containing pressures and sources at discrete points, respectively. The discrete analog to inequality (3) is that $\boldsymbol{M}^{-1}$ should be monotone (all matrix entries should be greater or equal to zero). Recent work has shown that this is frequently not the case [12,13].

One potential hazard of this non-monotone behavior is that unphysical instabilities with respect to the oil and gas equilibrium may arise [10]. This is sketched in Fig. 1, where a non-physical maximum occurs. If the pressure of the oil phase in some part of the reservoir is close to the bubble point pressure, dissolved gas may then appear when it should not be present. In both [12,13] different grids are investigated, and it is shown that there exist grids for which both the standard MPFA methods (the O- and U-methods) produce coefficient matrices with a non-monotone inverse. For general cases these grids may have moderate aspect ratios combined with random perturbations of the corners of rectangular grids, even with homogeneous isotropic permeability.

This paper will mainly focus on a new MPFA method, which is designed to enhance the monotonicity for cases known to cause problems for MPFA methods. The new method will fit into the same framework as the O-method, and the difference between the O-method and the new method is that other interaction regions will be used.

The rest of the paper is organized as follows: In Section 2, we review the principles behind the MPFA methods, and in particular the MPFA O-method transmissibilities are derived for a general matching quadrilateral grid in two dimensions. Section 3 presents the proposed MPFA Z-method in detail for quadrilaterals in two dimensions, and the transmissibilities are derived. A worked example is provided in Section 4, where the Z-method is applied on a parallelogram grid on a homogeneous medium. This section also contains analytical monotonicity results for parallelogram grids. General quadrilateral grids are discussed in Section 5, and a distance algorithm is proposed for combining the Z-method and the O-method on an entire grid. The algorithm is valid for both homogeneous, heterogeneous and anisotropic cases. Section 6 provides numerical examples that validate the improved discretization for simple solutions. In particular, uniform flow is shown to be reproduced exactly, and close to second order convergence is indicated for a piecewise quadratic reference solution on a layered medium with severe permeability anisotropy. Further numerical results are provided in Section 7, where the emphasis is on monotonicity of the discretization on grids relevant for field simulations. Finally, Section 8 contains conclusions and a summary.

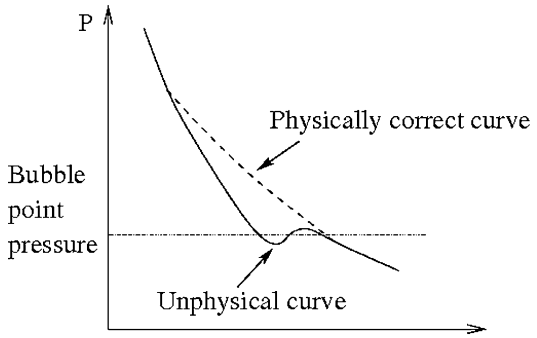

Fig. 1. Function with non-physical maximum resulting in unexpected gas occurrence. Variation along the abscissa can represent either time or spacial variables.

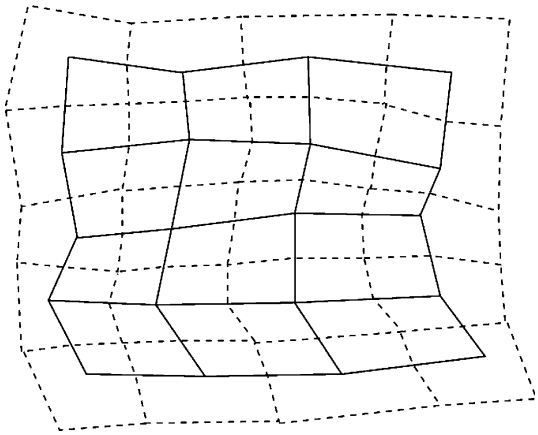

Fig. 2. Entire control volume grid. Control volumes shown by solid lines, interaction regions (dual grid) indicated by dashed lines.

2. Multi-point flux approximation methodology

All MPFA methods aim to calculate fluxes across cell interfaces (or parts thereof) by combining pressure values of neighboring cells, or cells that are in the vicinity of an interface. This is to improve on flux discretizations which only combine pressures from two neighboring grid cells (two point flux approximations). Such discretizations are generally not valid for grids which are skewed or have general full tensor permeability descriptions. Numerical results which show this are presented in [3,11]. The MPFA discretization approaches have been presented in detail in [1–17], and good introductions to the methodology can be found in [10,14]. Only a short summary of the methodology will be given here.

The two-dimensional case for general matching quadrilateral grid cells is illustrated in Fig. 2. The figure shows a quadrilateral grid (control volumes) for which a dual grid is constructed (dashed lines). The dual grid cells are called interaction regions, and will define which node pressure values to use for the discrete fluxes. In particular, four node pressures will be used to express discrete fluxes across the sub-interfaces within an interaction region in two dimensions. Fig. 3 shows four neighboring cells and an interaction region for a typical non-orthogonal grid. Four grid cells meet in each corner of a matching grid; furthermore, four cell interfaces meet at the corners, and four sub-interfaces are therefore contained in the interaction regions. The common corner is denoted the cluster center of the interaction region. Transmissibilities are calculated for each of the four sub-interfaces which meet at the corner. The transmissibilities $t_{i,j}$ are the node pressure weighting factors in a discrete flux approximation, as in the equation

$$f_i = \sum_{j=1}^{4} t_{i,j} u_j. \tag{5}$$

Here f_i is the flux across sub-interface e_i, while u_j is the pressure at node $\boldsymbol{x}_j$ of the interaction region.

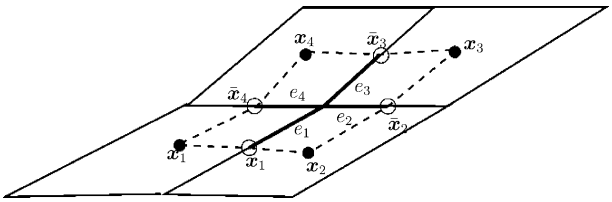

Fig. 3. Interacting cells for O-method; control volumes indicated by solid lines, interaction region by dashed lines, nodes $\boldsymbol{x}_1,\ldots,\boldsymbol{x}_4$ by dots, and dividing points $\bar{\boldsymbol{x}}_1,\ldots,\bar{\boldsymbol{x}}_4$ by circles.

The transmissibility calculations are based on the local information in an interaction region. For each of the four sub-interfaces, the continuous fluxes are given by

$$f_i = -\int_{S_i} \boldsymbol{K}\nabla u \cdot \boldsymbol{n}_i \mathrm{d}A, \tag{6}$$

where the entities are as follows: S_i is sub-interface e_i, $\boldsymbol{K}$ is the permeability of the specific cell and $\boldsymbol{n}_i$ is the outer unit normal of S_i.

By the assumption that pressures are piecewise linear on each sub-cell in the interaction region, it follows that ∇u is piecewise constant within it. The discrete fluxes that follow from Eq. (6) are hence constant, and using the information about ∇u on both sides (indicated by + and −) of the sub-interfaces leads to one flux continuity requirement for each sub-interface e_i. I.e.

$$f_{i-} = f_{i+} \tag{7}$$

for each sub-interface e_i implies that

$$-\boldsymbol{K}_{i-}\nabla u_{i-}\boldsymbol{n}_i = -\boldsymbol{K}_{i+}\nabla u_{i+}\boldsymbol{n}_i. \tag{8}$$

The transmissibility calculation is completed by a relaxed pressure continuity assumption [10]. For the O-method the pressures will be assumed to be continuous at each of the four dividing points $\bar{\boldsymbol{x}}_1, \ldots, \bar{\boldsymbol{x}}_4$, and these points will therefore be referred to as the pressure continuity points. These pressure continuity points together with the nodes will be used to evaluate the gradients of Eq. (8). We now have 12 restrictions (four node pressures at $\boldsymbol{x}_1,\ldots,\boldsymbol{x}_4$, four pressure continuity points $\bar{\boldsymbol{x}}_1, \ldots, \bar{\boldsymbol{x}}_4$, and four flux continuity conditions over sub-interfaces from Eq. (8)). These balance the 12 degrees of freedom from the linear pressure variation on each of the sub-cells.

To express a gradient by the three points associated with cell j, it is convenient to introduce vectors $\boldsymbol{v}_{jk}$, $k = 1,2$:

$$\boldsymbol{v}_{j1} = \boldsymbol{R}(\bar{\boldsymbol{x}}_{j2} - \boldsymbol{x}_j), \quad \boldsymbol{v}_{j2} = -\boldsymbol{R}(\bar{\boldsymbol{x}}_{j1} - \boldsymbol{x}_j), \tag{9}$$

where the second index refers to the local numbering of dividing points in a right handed system. Further, the matrix $\boldsymbol{R}$ is the rotation matrix given by

$$\boldsymbol{R} = \begin{bmatrix} 0 & -1 \\ 1 & 0 \end{bmatrix}. \tag{10}$$

Then the gradient can be expressed by [10]:

$$\nabla u_j = \sum_{k=1}^{2} \left(\frac{1}{T_j} \boldsymbol{v}_{jk} (\bar{u}_{jk} - u_j) \right). \tag{11}$$

The quantity T_j is the area of the triangle $(\boldsymbol{x}_j\bar{\boldsymbol{x}}_{j1}\bar{\boldsymbol{x}}_{j2})$, and is referred to as a variational triangle in MPFA terminology [10]. As examples of the double indexed variables, $\bar{u}_{12}$ is the pressure at the point $\bar{\boldsymbol{x}}_4$, $\boldsymbol{v}_{11}$ is the inward normal vector of the segment $\boldsymbol{x}_1\bar{\boldsymbol{x}}_4$, and $\boldsymbol{v}_{12}$ is the inward normal vector of the segment $\boldsymbol{x}_1\bar{\boldsymbol{x}}_1$.

Denoting the vector of the node pressures $\boldsymbol{u} = [u_1, u_2, u_3, u_4]^{\mathrm{T}}$ and the vector of dividing point pressures $\boldsymbol{v} = [\bar{u}_1, \bar{u}_2, \bar{u}_3, \bar{u}_4]^{\mathrm{T}}$, the four flux continuity requirements (7) may be rewritten in terms of these:

$$\boldsymbol{A}\boldsymbol{v} = \boldsymbol{B}\boldsymbol{u}. \tag{12}$$

The matrices $\boldsymbol{A}$ and $\boldsymbol{B}$ are 4×4 and consist of scalar coefficients, defined by

$$\omega_{ijk} = \frac{-\boldsymbol{n}_i \boldsymbol{K}_j \boldsymbol{v}_{jk}}{T_j}, \tag{13}$$

where the quantities are the same as defined above.

The matrix $\boldsymbol{A}$ will generally be invertible [8], and the dividing point pressures may therefore be eliminated to obtain

$$\boldsymbol{v} = \boldsymbol{A}^{-1}\boldsymbol{B}\boldsymbol{u}. \tag{14}$$

As explained in detail in [10] the left-hand side of the system (7) can be written as

$$\boldsymbol{f} = \boldsymbol{C}\boldsymbol{v} - \boldsymbol{D}\boldsymbol{u}, \tag{15}$$

where $\boldsymbol{C}$ and $\boldsymbol{D}$ are 4×4 (also consisting of scalar coefficients (13)). From Eqs. (14) and (16) it follows that the O-method fluxes may be expressed as

$$\boldsymbol{f} = (\boldsymbol{C}\boldsymbol{A}^{-1}\boldsymbol{B} - \boldsymbol{D})\boldsymbol{u}, \tag{16}$$

and the transmissibility matrix is therefore

$$\boldsymbol{T} = \boldsymbol{C}\boldsymbol{A}^{-1}\boldsymbol{B} - \boldsymbol{D}.$$

Each row of this matrix gives the node pressure weights in the flux approximation of the associated edge, corresponding to the transmissibilities of Eq. (5). The details of the calculations and explicit expressions for matrices $\boldsymbol{A}$, $\boldsymbol{B}$, $\boldsymbol{C}$ and $\boldsymbol{D}$ can be found in [10]. An assembly procedure can now be performed to construct the global system (4) from the local transmissibility matrices $\boldsymbol{T}$.

The boundary of the domain will readily be handled by defining an outer layer of artificial grid cells [2,4,5]. The interaction regions that cover the physical boundary of a domain will then contain two or more artificial grid cells. No-flow boundary conditions are easily implemented by assuming that the artificial cells are inactive, such that the fluxes across the corresponding interfaces are zero. More general boundary conditions for the MPFA O-method have also been handled in [11].

In Section 3, we present the flux discretization for the proposed Z-method. The method will use alternative interaction regions to the interaction regions used by the O-method. Z-method interaction regions with associated grid cells are shown in Fig. 4.

3. Derivation of the Z-method

The problems related to monotonicity observed in [12,13] indicate that on isotropic media, grid skewness may not always be handled properly by MPFA methods.

In [12] the nine-point cell stencil arising from a general control volume (CV) method is investigated, and sufficient criteria are derived for the method to satisfy monotonicity of the inverse operator for homogeneous parallelogram grids. A worked example is given, which discusses the MPFA O-method

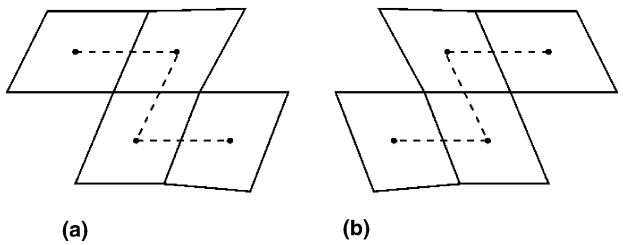

Fig. 4. Grid points and cells involved in the Z-method: (a) stylized Z; (b) stylized mirrored Z.

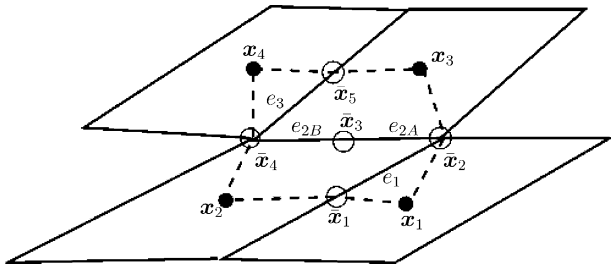

Fig. 5. Interacting cells for a Z-method; control volumes indicated by solid lines, interaction region by dashed lines, nodes $\boldsymbol{x}_1,\ldots,\boldsymbol{x}_4$ by dots, and dividing points $\bar{\boldsymbol{x}}_1,\ldots,\bar{\boldsymbol{x}}_5$ by circles.

discretization. The monotonicity of the inverse coefficient matrix depends on the internal angles of the parallelograms and the aspect ratios. For aspect ratios close to unity and angles less than 45°, the O-method fails to produce a coefficient matrix with a positive inverse. For large aspect ratios (which is frequently encountered in reservoir simulation), severe restrictions apply to the parallelogram angles in order to secure monotonicity. These results may be explained geometrically (for the O-method) by the fact that the interacting cells may be located too far from each other when the acute parallelogram angle is small.

The above discussion motivates the development of the Z-method, as seen on a two-dimensional skew grid as in Fig. 5. Here, the suggested interaction region is constrained by four grid cells which are not the logical neighbors as used by the O- and U-methods. The choice of cells will be further discussed in Section 5. The discretization makes use of the nodes $\boldsymbol{x}_1,\ldots,\boldsymbol{x}_4$, and the dividing points $\bar{\boldsymbol{x}}_1,\ldots,\bar{\boldsymbol{x}}_5$, and the name is derived from the stylized Z (or mirrored Z) which connects the nodes of the interacting cells as in Fig. 4. It should be clear from comparing Figs. 3 and 5 that for very skew grid cell configurations and large aspect ratios the Z-method can be considered a more natural discretization.

In the development that follows, we solely concern ourselves with discretizations in two dimensions. While the ideas presented can be extended to three dimensions, this has not been implemented yet.

The details of the Z-method transmissibility calculations use notation from Fig. 5. The three sub-interfaces (e_1, e_2, e_3) and the four nodes ($\boldsymbol{x}_1,\ldots,\boldsymbol{x}_4$) are used for flux calculations as well as the five additional points ($\bar{\boldsymbol{x}}_1,\ldots,\bar{\boldsymbol{x}}_5$) which are the pressure continuity points. In the following, e_2 will refer to either sub-interface e_{2A} or e_{2B}; the choice of sub-interface will not affect the calculations. In each of the four interacting cells in Fig. 5 we assume that the pressure variation is linear in sub-cells made up by the cell node and two or three associated pressure continuity points. As an example, the sub-cell used for cell 1 uses the node $\boldsymbol{x}_1$ and the continuity points $\bar{\boldsymbol{x}}_1$ and $\bar{\boldsymbol{x}}_2$, while cell 2 uses the node $\boldsymbol{x}_2$ and the continuity points $\bar{\boldsymbol{x}}_1, \bar{\boldsymbol{x}}_2$ and $\bar{\boldsymbol{x}}_3$.

Flux continuity is posed for the three sub-interfaces labeled $e_1,\ldots,e_3$, and an equivalent system to Eq. (8) is obtained. We also impose full pressure continuity across sub-interfaces e_1 and e_3, while only continuity at the point $\bar{\boldsymbol{x}}_3$ for the sub-interface e_2. In total, this yields 12 conditions on the discrete pressure variation (four node pressures at $\boldsymbol{x}_1,\ldots,\boldsymbol{x}_4$, five pressure continuity points $\bar{\boldsymbol{x}}_1,\ldots,\bar{\boldsymbol{x}}_5$, and three flux continuity conditions over sub-interfaces). In addition to these flux and pressure continuity conditions, the node pressure and three dividing point pressures in cells 2 and 3 are related by the linear pressure variation in each sub-cell. These relationships are consequences of the linear pressure variation, and hence do not restrict the pressure variation further.

Denoting the vectors $\boldsymbol{u} = [u_1, u_2, u_3, u_4]^{\mathrm{T}}$ as the pressures at the cell nodes, and $\boldsymbol{v} = [\bar{u}_1, \bar{u}_2, \bar{u}_3, \bar{u}_4, \bar{u}_5]^{\mathrm{T}}$ as the pressure at the dividing points, the local system of flux continuity conditions and pressure relations is given by Eq. (12). For the Z-method depicted in Fig. 5, the 5×5 matrix $\boldsymbol{A}$ and 5×4 matrix $\boldsymbol{B}$ are given by

$$\boldsymbol{A} = \begin{bmatrix} \omega_{111} - \omega_{122} & \omega_{112} & -\omega_{121} & 0 & -0 \\ -\omega_{222} & 0 & \omega_{232} - \omega_{221} & 0 & \omega_{232} \\ 0 & 0 & \omega_{331} & -\omega_{342} & \omega_{332} - \omega_{341} \\ a_{41} & a_{42} & a_{43} & 0 & 0 \\ 0 & 0 & a_{53} & a_{54} & a_{55} \end{bmatrix}, \tag{17}$$

and

$$\boldsymbol{B} = \begin{bmatrix} \omega_{111} + \omega_{112} & -\omega_{121} - \omega_{122} & 0 & 0 \\ 0 & -\omega_{221} - \omega_{222} & \omega_{231} + \omega_{232} & 0 \\ 0 & 0 & \omega_{331} + \omega_{332} & -\omega_{341} - \omega_{342} \\ 0 & b_{42} & 0 & 0 \\ 0 & 0 & b_{53} & 0 \end{bmatrix}. \tag{18}$$

The elements of row 4 and 5 of $\boldsymbol{A}$ and $\boldsymbol{B}$ are the relations among the pressures at nodes and dividing points in cell 2 and 3 of Fig. 5 due to the linear pressure approximation inside each cell:

$$\bar{u}_2 + \frac{1}{|\boldsymbol{x}_2 - \bar{\boldsymbol{x}}_2|}|\boldsymbol{\xi}_1 - \bar{\boldsymbol{x}}_2|(u_2 - \bar{u}_2) = \bar{u}_1 + \frac{1}{|\bar{\boldsymbol{x}}_3 - \bar{\boldsymbol{x}}_1|}|\boldsymbol{\xi}_1 - \bar{\boldsymbol{x}}_1|(\bar{u}_3 - \bar{u}_1), \tag{19}$$

and

$$\bar{u}_4 + \frac{1}{|\boldsymbol{x}_3 - \bar{\boldsymbol{x}}_4|}|\boldsymbol{\xi}_2 - \bar{\boldsymbol{x}}_4|(u_3 - \bar{u}_4) = \bar{u}_3 + \frac{1}{|\bar{\boldsymbol{x}}_5 - \bar{\boldsymbol{x}}_3|}|\boldsymbol{\xi}_2 - \bar{\boldsymbol{x}}_3|(\bar{u}_5 - \bar{u}_3). \tag{20}$$

The additional points $\boldsymbol{\xi}_1$ and $\boldsymbol{\xi}_2$ are the diagonal intersections of the quadrilaterals $(\boldsymbol{x}_2, \bar{\boldsymbol{x}}_1, \bar{\boldsymbol{x}}_2, \bar{\boldsymbol{x}}_3)$ and $(\boldsymbol{x}_3, \bar{\boldsymbol{x}}_3, \bar{\boldsymbol{x}}_4, \bar{\boldsymbol{x}}_5)$, respectively.

Again the left-hand side of Eq. (8) may be used to write the three sub-interface fluxes as functions of the node pressures and the dividing point pressures:

$$\boldsymbol{f} = \boldsymbol{C}_{3\times 5}\boldsymbol{v} - \boldsymbol{D}_{3\times 4}\boldsymbol{u}, \tag{21}$$

where the indexing of the matrices $\boldsymbol{C}$ and $\boldsymbol{D}$ states their sizes. Equivalently to Eq. (16) we can now write out the discrete flux

$$\boldsymbol{f} = (\boldsymbol{C}_{3\times 5}\boldsymbol{A}^{-1}\boldsymbol{B} - \boldsymbol{D}_{3\times 4})\boldsymbol{u}, \tag{22}$$

where each line of Eq. (22) corresponds to an instantation of Eq. (5).

The sub-interface fluxes can be combined to construct the coefficient matrix which corresponds to the continuous operator $\mathscr{L}(\mu) = -\int \nabla \cdot (\boldsymbol{K}\nabla\mu)\,\mathrm{d}V$ on each cell by combining appropriate elements of $\boldsymbol{f}$ from Eq. (22).

4. Worked example of Z-method

We now present the Z-method for the case of uniform parallelogram grids, with an interaction region with the logical shape of e.g. cells 1, 2, 4 and 9 in Fig. 6(a). Three other Z-method molecules could equally well be chosen instead, based on rotation and symmetry. We will later choose the interaction region on which to base the discretization, according to the skewness and aspect ratio of the grid and the anisotropy of the medium. This will be further discussed in Section 5.

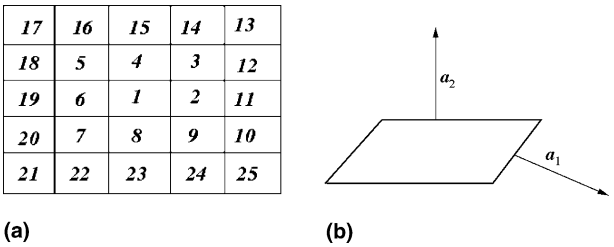

Fig. 6. Parallelogram cell (b) and local numbering (a) of cells in cluster.

The parallelogram grid cells are described by the vectors $\boldsymbol{a}_1$ and $\boldsymbol{a}_2$ in Fig. 6(b). These vectors are normal to the edges of the parallelogram, scaled such that $\boldsymbol{a}_i$ equals the length of the edge. The local system of equations may then be written out explicitly by coefficients that are combinations of the following three parameters

$$a = \frac{1}{V}\boldsymbol{a}_1^{\mathrm{T}}\boldsymbol{K}\boldsymbol{a}_1, \quad b = \frac{1}{V}\boldsymbol{a}_2^{\mathrm{T}}\boldsymbol{K}\boldsymbol{a}_2, \quad c = \frac{1}{V}\boldsymbol{a}_1^{\mathrm{T}}\boldsymbol{K}\boldsymbol{a}_2. \tag{23}$$

The system of flux continuity equations (8) approximated using Eq. (11) then reads

$$\begin{aligned} &b(\bar{u}_1 - u_1) - c(\bar{u}_2 - \bar{u}_1) = -c(\bar{u}_3 - u_2) - b(\bar{u}_1 - u_2),\\ &a(\bar{u}_3 - u_2) + c(\bar{u}_1 - u_2) = c(u_3 - \bar{u}_5) - a(\bar{u}_3 - u_3),\\ &b(\bar{u}_5 - u_4) - c(\bar{u}_4 - \bar{u}_5) = -c(\bar{u}_3 - u_3) - b(\bar{u}_5 - u_3). \end{aligned} \tag{24}$$

In addition, Eqs. (19) and (20) simplify to

$$\begin{aligned} &\bar{u}_1 + \bar{u}_3 - (\bar{u}_2 + u_2) = 0,\\ &\bar{u}_5 + \bar{u}_3 - (u_3 + \bar{u}_4) = 0. \end{aligned} \tag{25}$$

If we combine Eqs. (24) and (25), as in Section 3, we then arrive at the transmissibilities:

$$\boldsymbol{T} = \frac{1}{4a}\begin{bmatrix} c^2 - 2ab & 2ab + 2ac - c^2 & -c^2 - 2ac & c^2\\ -ac & ac + 2a^2 & -ac - 2a^2 & ac\\ -c^2 & c^2 + 2ac & -2ab - 2ac + c^2 & -c^2 + 2ab \end{bmatrix}. \tag{26}$$

When combined into discrete (full) edge fluxes, we get in the i-direction:

$$f_{1,2} = -2(t_{2,1}u_9 + t_{2,2}u_2 + t_{2,3}u_1 + t_{2,4}u_4) = \left(a + \frac{c}{2}\right)(u_1 - u_2) - \frac{c}{2}(u_4 - u_9), \tag{27}$$

and similarly in the j-direction

$$\begin{aligned} f_{1,4} &= -((t_{1,1} + t_{3,3})u_1 + (t_{1,2} + t_{3,4})u_4 + t_{1,3}u_5 + t_{3,2}u_2 + t_{1,4}u_{16} + t_{3,1}u_9)\\ &= \left(b + \frac{c}{2} - \frac{c^2}{2a}\right)(u_1 - u_2) - \left(\frac{c}{2} + \frac{c^2}{4a}\right)(u_5 - u_3) - \frac{c^2}{4a}(u_{16} - u_9). \end{aligned} \tag{28}$$

Here the $t_{i,j}$ are the elements of $\boldsymbol{T}$, $f_{i,j}$ refers to the flux between cells i and j, and u_i refers to the pressure in cell i. The cells are numbered as in Fig. 6(a). We now combine $f_{1,2}$, $f_{1,4}$, $f_{1,6}$ and $f_{1,8}$ to obtain a nine-point stencil, with weights m_i. The elements of the coefficient matrix $\boldsymbol{M}$ in Eq. (4) are those of the nine-point stencil,

$$m_2 = -a - c - \frac{c^2}{4a}, \quad m_4 = -b - c + \frac{c^2}{2a}, \quad m_5 = c + \frac{c^2}{2a}, \quad m_{16} = -\frac{c^2}{4a}. \tag{29}$$

The numbering again refers to Fig. 6(a). The coefficient matrix is symmetric such that $m_6 = m_2$, $m_8 = m_4$, $m_9 = m_5$ and $m_{24} = m_{16}$. To retain zero flow on constant pressure fields, $m_1 = -\text{sum}_{i\neq 1}$, where all m_i not defined above equal zero. Note that m_{16} and m_{24} are weightings of cells outside the inner nine cells used by traditional nine-point discretizations, while the cells m_7 and m_3 are not used.

For the parallelogram grid, the system matrix arising from the Z-method may be compared to the corresponding matrix obtained from the O-method. The coefficients m_i for the O-method may be found in either [10] or [12]. Since $a > 0$ from the definition in Eq. (23) it follows that

$$\text{sign}(\boldsymbol{M}^{-1}) = \text{sign}((\boldsymbol{M}/a)^{-1}). \tag{30}$$

We therefore study the matrix $\boldsymbol{M}' = \boldsymbol{M}/a$. From Eq. (29) we observe that this matrix is a function of only two parameters b/a and c/a. Further, the invertibility of the definitions of a, b, and c lets us consider the matrix $\boldsymbol{M}'$ as a function of the coordinates of either $\boldsymbol{a}_1$ or $\boldsymbol{a}_2$. Together with the choice of Z-method according to Section 5, we therefore choose, without loss of generality, the media to be isotropic, $\boldsymbol{a}_2 = [-1,0]^{\mathrm{T}}$, and $\|\boldsymbol{a}_1\| < 1, \boldsymbol{a}_1 = [a_{1,1}, a_{1,2}]^{\mathrm{T}}$, $a_{1,i} \geqslant 0$. Our two variables are then the two coordinates of $\boldsymbol{a}_1$. Every grid point in Fig. 7(a) represents the vector $\boldsymbol{a}_1 = [a_{1,1}, a_{1,2}]^{\mathrm{T}}$, such that Ω_1 is the region containing parallelogram grids where both Z- and O-methods have monotone inverses. Conversely, both methods have non-monotone inverses in the regions labeled Ω_4. The intermediate regions where only the Z- or O- methods have the desired monotone properties are denoted as Ω_2 and Ω_3, respectively. The region Ω_5 outside the unity circle can be disregarded based on the symmetry of the discretization with respect to $\boldsymbol{a}_1$ and $\boldsymbol{a}_2$. The region $\|\boldsymbol{a}_1\| < 0.1$ (high aspect ratios or severe anisotropy) is particularly interesting with respect to reservoir simulation, and a more detailed view of this region is shown in Fig. 7(b).

It should also be pointed out that for $c = 0$, termed K-orthogonality in [10], the coefficients in relations Eq. (29) are all less than or equal to zero. This implies that the system matrix is an M-matrix, and its inverse is monotone. A matrix $\boldsymbol{A}$ is an M-matrix if and only if the entries $a_{i,j}$ satisfy [37]:

$$a_{i,i} > 0 \quad \forall i, \tag{31a}$$

$$a_{i,j} \leqslant 0 \quad \forall i, j, \ \ i \neq j, \tag{31b}$$

$$\sum_i d_i a_{i,j} \geqslant 0 \quad \forall j, \tag{31c}$$

with strict inequality for at least one of Eqs. (31c) and some positive vector d. Further, when $c = -2a$, $m_2 = m_5 = 0$, the Z-method discretization reduces to a five-point scheme, which is also an M-matrix. In fact,

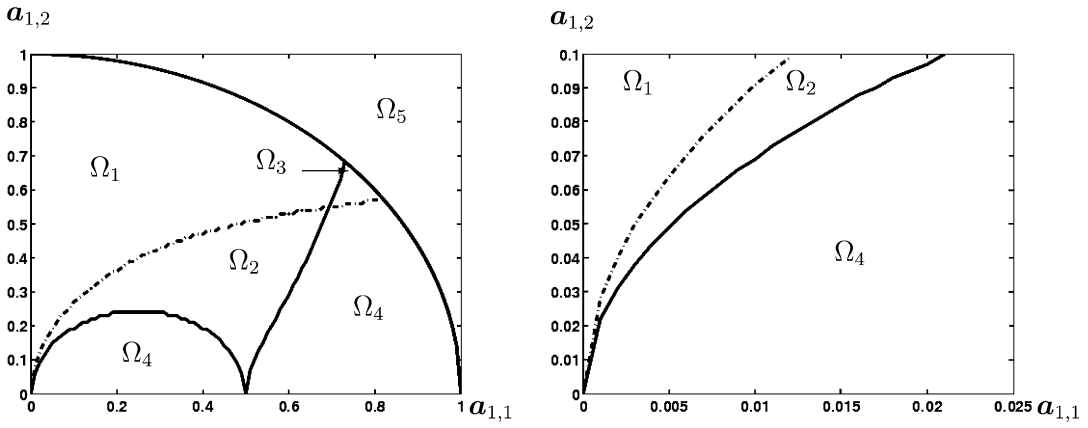

Fig. 7. Monotonicity regions for the MPFA Z-method (dashed lines) and the O-method (continuous lines).

while the system matrix arising from an O-method is never an M-matrix for $c \neq 0$, the system matrix arising from the Z-method discretization is an M-matrix in the in the entire regions Ω_1 and Ω_2 of Fig. 7.

To see the extent of where the Z-method system matrix is an M-matrix, recall that M-matrices require all non-diagonal elements to be non-positive. We use the elementary properties $a > 0$, $b > 0$ and $|c| < \max(a,b)$. The interaction region chosen in this worked example (cells 1, 2, 4 and 9 in Fig. 6(a)) seems ideal when $c \leqslant 0$ and $a \leqslant b$. Then the M-matrix constraints $m_i \leqslant 0$ from Eq. (31b) then imply that

$$c \geqslant -2a, \quad c \geqslant a - \sqrt{a^2 + 2ab}, \tag{32}$$

are the conditions that must be met if the system matrix is to be an M-matrix. For grids where $c \geqslant 0$ or $a \geqslant b$, symmetry arguments define the appropriate rotation or reflection of the Z-method and corresponding constraints. We conclude that when

$$|c| \leqslant 2\min(a, b) \tag{33a}$$

and

$$|c| \leqslant \min(\sqrt{a^2 + 2ab} - a, \sqrt{b^2 + 2ab} - b), \tag{33b}$$

there exists a Z-method discretization for which the system matrix is an M-matrix.

5. Selection algorithm for general grids

In the previous section, we observed that the Z-method satisfies monotonicity properties for a larger set of grids than the O-method. However, on less skewed grids, both Z- and O-method discretizations have monotone inverses. The motivation for the Z-method is the location of the nodes close to the sub-interface over which we want to evaluate fluxes. Thus it is natural that when the grid skewness is small, there is no need for the Z-method interaction region. Therefore, we propose to combine the Z- and O-methods based on closest point properties.

5.1. Homogeneous cases

We perform the combined flux calculations by the following ideas: For each inner corner of the grid, transmissibilities will be calculated for each of the four sub-interfaces that meet in the grid corner. Each sub-interface is a part of a whole edge, such that a whole edge is divided in two equal parts, which are then assigned to two opposite corners. The four sub-interfaces belonging to a specific corner x_k are shown in Fig. 8(a). Each sub-interface is successively defined as a central edge for transmissibility calculations, similar to the procedure in [5].

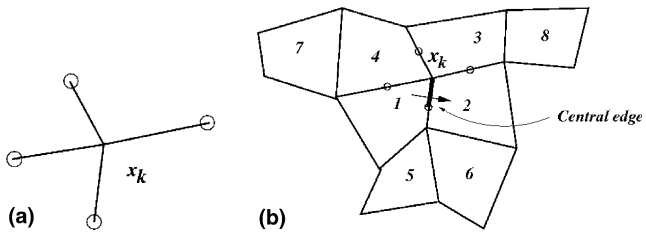

Fig. 8. (a) Corner x_k with four associated sub-interfaces. (b) Eight cells are candidates for interacting cells to determine transmissibilities for the central edge.

For each of the sub-interfaces the transmissibilities may be evaluated by either the O-method or the Z-method. The situation for the first local sub-interface belonging to the corner $\boldsymbol{x}_k$ is shown in Fig. 8(b). Eight cells are candidates for being the four interacting cells that determine the flux across this edge. The distance from each cell node of the candidate cells 3–8 to the corner $\boldsymbol{x}_k$ determines which discretization should be applied. If either cell 5, 6, 7 or 8 is closest, a Z-molecule involving this cell should be applied. If cell 3 is closest, and cell 5 or 8 are second closest, then the Z-molecule involving the two closest cells should be used. The same holds if cell 4 is closest and cell 6 or 7 are second closest. In all other cases the O-method should be preferred. This will be the case for the example depicted in Fig. 8(b).

5.2. Extension to heterogeneous media

The geometric distance in Section 5.1 may be generalized to account for heterogeneous and anisotropic cases. We accomplish this by scaling the distance by the inverse of the permeability matrix. The distance from the cluster center to the nodes that are not nearest neighbor cells then consists of two terms. As an example, the distance function for local cell 5 in the cell configuration depicted in Fig. 8 is given by

$$d_5 = \min_{\boldsymbol{x}_I \in e_{1,5}} \left(|(\boldsymbol{K}_1^{-1}(\boldsymbol{x}_I - \boldsymbol{x}_C)| + |\boldsymbol{K}_5^{-1}(\boldsymbol{x}_I - \boldsymbol{x}_5)| \right). \tag{34}$$

The point $\boldsymbol{x}_C$ is the cluster center, $\boldsymbol{x}_5$ is the node of cell 5 and $e_{1,5}$ is the interface between cells 1 and 5. The minimum is taken over all points on the interface. This weighting function accounts for both heterogeneities and anisotropy, and using this general distance function for all eight nodes, the same selection algorithm as in Section 5.1 may be used. Note that this seems to be a reasonable first approach to handling general cases, but that even better selection approaches could be based on comparison of calculated transmissibilities by the different discretization methods. For very distorted grids and general permeabilities, the effective distances may not fully explain which discretization technique is the best locally.

For practical purposes we are limited to search for a minimum over a discrete set of points on the line segment $e_{1,5}$ in Eq. (34). However, keeping in mind that Eq. (34) is primarily an order of magnitude computation, this should not have significant effects on monotonicity. Numerical experiments where the precision in finding the minima is varied verify this claim.

6. Validation of the method

In this section, we focus on the treatment of uniform flow and convergence of known problems on challenging grids, which are relevant for reservoir simulation.

6.1. Uniform flow

All MPFA discretization methods defined on the physical space can be shown to have the property that the numerical solution of Eq. (1) is exact for uniform flow.

For the Z-method as formulated, the result follows from the observation that the system of Eqs. (21) has a unique solution, and that linear flow satisfies all Eqs. (12) due to the linear approximation of the gradient in Eq. (11). The result is intuitive, but a stringent proof is given in [11] for the O-method. The result can also be extended to the case of piecewise uniform flow, using the ideas in the proof for reproduction of uniform flow in [11].

When the O-method and Z-method are combined, the same result holds, and a specific case is shown in Fig. 9, where the pressure field with $\nabla u = [1,0]^{\mathrm{T}}$ is applied on a selected grid which resembles relevant

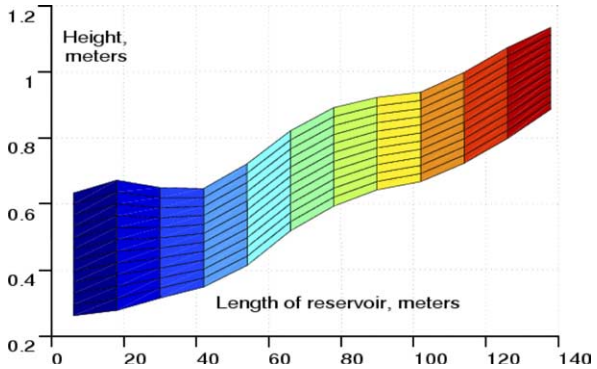

Fig. 9. Numerical solution for test example; uniform flow in x-direction.

geometry for a North Sea reservoir. The discretization uses the selection algorithm described in Section 5.1, and roughly 47% of the half edges are handled by the Z-method.

6.2. Convergence

A wide range of numerical convergence examples for the MPFA O-method can be found in [11]. Those examples are both for homogeneous and heterogeneous cases, and second order convergence of pressure and normal fluxes is observed for smooth solutions. Comparison of MPFA methods with other established methods has been undertaken in previous studies [38,39]. For this short validation of the Z-method, we will therefore limit ourselves to comparison of pressure convergence with the MPFA O-method. We choose an example from [15], where the medium is layered, and the anisotropic permeabilities are given by

$$\boldsymbol{K}_{\mathrm{l}} = \begin{bmatrix} 50 & 0 \\ 0 & 1 \end{bmatrix}, \quad \boldsymbol{K}_{\mathrm{r}} = \begin{bmatrix} 1 & 0 \\ 0 & 10 \end{bmatrix}. \tag{35}$$

The analytical solution for this problem is piecewise quadratic, and we solve the discrete problem on grids which contain skew grid cells; one refinement level is depicted in Fig. 10. The permeabilities $\boldsymbol{K}_{\mathrm{l}}$ apply for the cells to the left of the grid line $x = 1/2$, and $\boldsymbol{K}_{\mathrm{r}}$ apply for the cells to the right of $x = 1/2$. Boundary conditions are implemented by specifying the exact pressures at nodes in an artificial layer of grid cells that surround

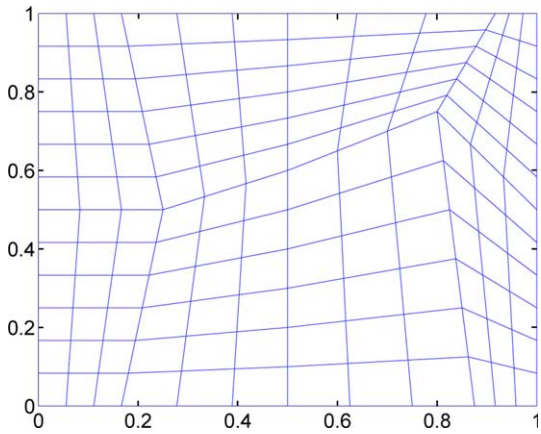

Fig. 10. One grid refinement level; piecewise quadratic problem solved on grid sequence.

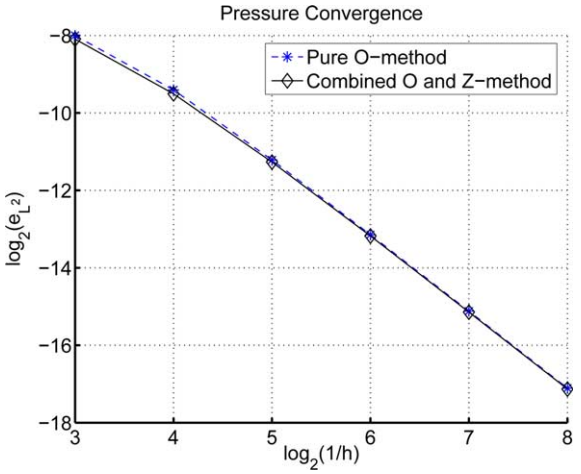

Fig. 11. Convergence behavior for a piecewise quadratic solution; L_2 error vs. refinement level. The combined O- and Z-methods perform slightly better than the pure O-method in terms of the L_2 error.

the entire domain. This is for convenience only, and general Dirichlet boundary condition can easily be implemented by the ideas in [11].

The convergence behavior for the pressure for uniform refinement of the grid is shown in Fig. 11, where six levels of refinement are included. The error is measured in the discrete L_2-norm given by

$$e_{\mathscr{P}_2} = \left(\sum_i (A_i (p_{\mathrm{ex},i} - p_i)^2) \right)^{1/2}, \tag{36}$$

where A_i is the area of grid cell i, $p_{\mathrm{ex},i}$ is the exact solution evaluated at node i, and p_i is the discrete pressure at node i; see [11] for details.

The observed convergence is practically h^2 for the last level of refinements for the combined O- and Z-methods, and the same is observed for the pure O-method. The L_2-errors are 5–6% smaller for the combined method in the earliest levels, but only 2–3% better in the last refinements. This is probably explained by the fact that the ratio of cell edges that apply the Z-method discretization is not constant throughout the refinement procedure.

7. Monotonicity results

In the following section, we compare the monotonicity properties of the classical O-method to the combined O- and Z-methods. The system matrix when we refer to the Z-method below is a combination of O-method and Z-method transmissibilities according to Section 5. The grids for which we investigate the proposed discretization are relevant for reservoir simulation, and both homogeneous and heterogeneous cases are included.

7.1. Homogeneous cases

Two-dimensional models may be used as simple models for North Sea Reservoirs. Characteristic geometry and geology for a realistic reservoir is indicated by the grid of Fig. 9. The grid cells may be very thin compared to the length and width of the cells; the aspect ratio is up to 200–300 after a correction

for anisotropy. For the specific example of Fig. 9, the coefficient matrix arising from the Z-method discretization is a matrix with a monotone inverse. The pure O-method does not give a coefficient matrix with a monotone inverse.

The Z-method discretization is now explored on a large set of such grids. We generate grid sequences where the length of the pillar lines (see [40]) of the grids are kept constant. The pillar lines are moved upwards linearly with an iteration parameter k, but with different velocities, such that the grid becomes skewer with the parameter k.

Our investigations are based on 1000 initial grids, where the lower boundary of each initial grid is a positive perturbation of a horizontal line. The limitations on the perturbations of the grids is that local dip downs (second order differences in pillar heights) should not exceed two grid cells.

The 1000 initial grids are skewed by the parameter k until non-monotone behavior is observed. The values of k for which the Z-method looses monotonicity of the inverse operator is shown in Fig. 12(a), and we see that we get approximately a Gaussian distribution. When comparing these results to the pure O-method, we use the quantity

$$g_i = \frac{k_{i,Z} - k_{i,O}}{k_{i,O}}. \tag{37}$$

The first subscript refers to the final iteration count that bounds the extent of monotonicity for the two methods, and the second subscript denotes the method. Therefore, g_i gives a measure of how much further the Z-method can be skewed than the O-method. The results are shown in Fig. 12(b), and we see that the improvement of the Z-method compared to the pure O-method peaks around 30%.

We should comment that to further improve the system matrices, the large aspect ratios may be reduced by refinement of the grid in the x-direction.

7.2. Layered media

The grids in Section 7.1 may also be used in combination with heterogeneity. As an example we investigate the grid in Fig. 9, where we divide the domain into three layers with permeabilities $\boldsymbol{K}_1 = 3\boldsymbol{I}$, $\boldsymbol{K}_2 = 8\boldsymbol{I}$ and $\boldsymbol{K}_3 = 7\boldsymbol{I}$, where the numbering of the layers is upwards. For this case, the dynamic transmissibility approach handles around 18% more grids than the O-method when the grid experiences the same variation as in Section 7.1. Experiments have also been performed with random permeability distributions of all 12

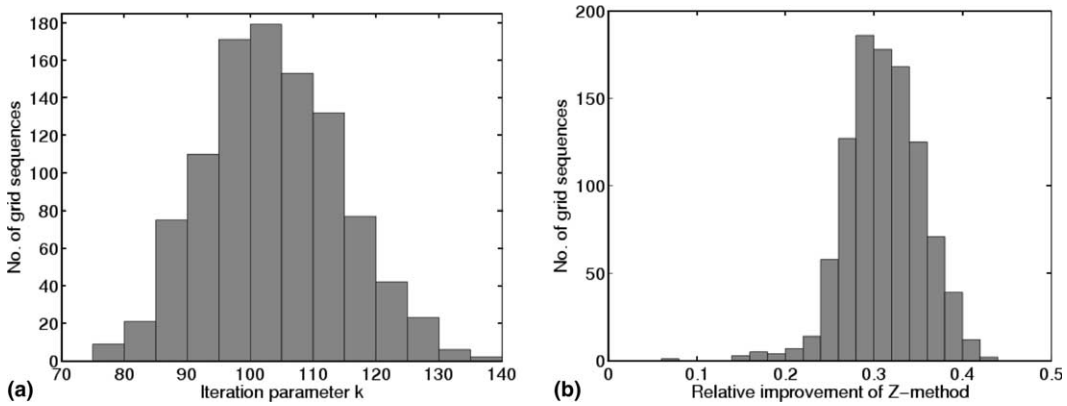

Fig. 12. (a) Distribution of iteration parameter when coefficient matrix becomes non-positive for Z-method. (b) Distribution of relative improvement of Z-method compared to the pure O-method.

layers of the grid. The same trends as above are observed in respect to the performance of the Z-method versus the pure O-method. For grids similar to the ones used here, we therefore conclude that the Z-method provides a better discretization than the O-method in terms of monotonicity, without loss of convergence.

8. Conclusions

In this paper, we have presented a new approach for generating MPFA transmissibilities for cases of skew grids. This transmissibility generation is used locally in grids where a distance criterium is used to choose either the O-method or the new Z-method. For parallelogram grids on homogeneous media the coefficient matrix given by the Z-method is not only inverse monotone for a wider range of grids than the O-method; it is also an M-matrix. This is in contrast to the O-method which only results in M-matrices on $\boldsymbol{K}$-orthogonal grids. The good monotonicity results are also observed in the extension to non-uniform grids.

Numerical results have been presented that shows an improvement of the MPFA discretization in respect to monotonicity. Convergence results for smooth solutions indicate that the method performs equally well as the O-method.

Acknowledgments

The first author was funded by the Norwegian Research Council and Norsk Hydro through Grant 151400/210. We thank our colleagues Ivar Aavatsmark and Runhild Klausen for useful discussions on MPFA methods.

References

[1] I. Aavatsmark, T. Barkve, Ø. Bøe, T. Mannseth, Discretization on non-orthogonal, curvilinear grids for multi-phase flow, in: Proceedings of the 4th European Conference on the Mathematics of Oil Recovery, vol. D, Røros, Norway, 1994, 17pp.
[2] I. Aavatsmark, T. Barkve, T. Mannseth, Ø. Bøe, Discretization on non-orthogonal, quadrilateral grids for inhomogeneous, anisotropic media, J. Comput. Phys. 127 (1996) 2–14.
[3] I. Aavatsmark, T. Barkve, Ø. Bøe, T. Mannseth, A class of discretization methods for structured and unstructured grids in anisotropic, inhomogeneous media, in: Proceedings of the 5th European Conference on the Mathematics of Oil Recovery, Leoben, Austria, 1996.
[4] I. Aavatsmark, T. Barkve, T. Mannseth, control-volume discretization methods for 3D quadrilateral grids in inhomogeneous, anisotropic reservoirs, SPE 38000.
[5] I. Aavatsmark, T. Barkve, Ø. Bøe, T. Mannseth, Discretization on unstructured grids for inhomogeneous anisotropic media. Part I: derivation of the methods, SIAM J. Sci. Comput. 18 (1998) 1700–1716.
[6] I. Aavatsmark, T. Barkve, Ø. Bøe, T. Mannseth, Discretization on unstructured grids for inhomogeneous, anisotropic media. Part II: discussion and numerical results, SIAM J. Sci. Comput. 19 (1998) 1717–1736.
[7] I. Aavatsmark, E. Reiso, R. Teigland, Control-volume discretization method for quadrilateral grids with faults and local refinement, Comput. Geosci. 5 (2001) 1–23.
[8] I. Aavatsmark, E. Reiso, H. Reme, R. Teigland, MPFA for faults and local refinement in 3D quadrilateral grids with application to field simulations, in: Proceedings of SPE Reservoir Simulation Symposium, SPE 66356, Houston, TX, 2001.
[9] G.T. Eigestad, I. Aavatsmark, E. Reiso, H. Reme, MPFA for faults with crossing grid lines and zig-zag patterns, ECMOR VIII, September 3–6, 2002.
[10] I. Aavatsmark, An introduction to multipoint flux approximations for quadrilateral grids, Comput. Geosci. 6 (2002) 405–432.
[11] G.T. Eigestad and R.A. Klausen, On the Convergence of the Multi-Point Flux Approximation O-method; Numerical Experiments for Discontinuous Permeability, submitted to Numerical Methods for Partial Differential Equations.
[12] J.M. Nordbotten, I. Aavatsmark, Monotonicity conditions for control volume methods on uniform parallelogram grids in homogeneous media, Comput. Geosci. (to appear).

[13] J.M. Nordbotten, G.T. Eigestad, Monotonicity conditions for control volume methods on general quadrilateral grids; application to MPFA, in: Proceedings of the 16th Nordic Seminar on Computational Mechanics.
[14] M.G. Edwards, C.F. Rogers, A flux continuous scheme for the full tensor pressure equation, in: Proceedings of the 4th European Conference on the Mathematics of Oil Recovery, Norway, June 1994.
[15] M.G. Edwards, C.F. Rogers, Finite volume discretization with imposed flux continuity for the general tensor pressure equation, Comput. Geosci. 2 (1998) 259–290.
[16] M.G. Edwards, M-matrix flux splitting for general full tensor discretization operators on structured and unstructured grids, J. Comput. Phys. 160 (2000) 1–28.
[17] H. Cao, Development of techniques for general purpose simulators, Ph.D. Thesis, Stanford University, 2002.
[18] S.C. Brenner, L. Ridgway Scott, The Mathematical Theory of Finite Element Methods, Springer, Berlin, 1994.
[19] G. Strang, G. Fix, An Analysis of the Finite Element Method, Wiley, New York, 1973.
[20] D. Braess, Finite Elements, Cambridge University Press, Cambridge, 2001.
[21] B. Riviere, M.F. Wheeler, K. Banas, Discontinuous Galerkin method applied to a single phase flow in porous media, Comput. Geosci. 4 (2000) 337–349.
[22] P.A. Forsyth, A Control-Volume, Finite-Element Method for Local Mesh Refinement in Thermal Reservoir Simulation, SPE Reservoir Engineering, SPE 18415, November 1990, pp. 561–566.
[23] R. Huber, R. Helmig, Node-centered finite volume discretizations for the numerical simulation of multiphase flow in heterogeneous porous media, Comput. Geosci. 4 (2) (2000) 141–164.
[24] F. Brezzi, M. Fortin, Mixed and Hybrid Finite Element Methods, Springer, New York, 1991.
[25] Z. Cai, J.E. Jones, S.F. McCormick, T.F. Russell, Control-volume mixed finite element methods, Comput. Geosci.. 1 (1997) 289–315.
[26] R.L. Naff, T.F. Russell, J.D. Wilson, Shape functions for velocity interpolation in general hexahedral cells, Comput. Geosci. 6 (2002) 285–314.
[27] D.N. Arnold, F. Brezzi, Mixed and nonconforming finite element methods: implementation, postprocessing and error estimates, Math. Modeling Numer. Anal. 19 (1985) 7–32.
[28] J.A. Wheeler, M.F. Wheeler, I. Yotov, Enhanced velocity mixed finite element methods for flow in multiblock domains, TICAM Report 01-27, September 2001.
[29] I. Yotov, Mixed finite element methods for flow in porous media, Ph.D. Thesis, Rice University, 1996.
[30] T.F. Russell, M.F. Wheeler, in: R. Ewing (Ed.), Finite Element and Finite Difference Methods for Continuous Flows in Porous Media, The Mathematics of Reservoir Simulation, SIAM, Philadelphia, 1983.
[31] S. Verma, K. Aziz, A control volume scheme for flexible grids in reservoir simulation, in: 14th SPE Reservoir Symposium, Dallas, TX, SPE 37999, June 1997.
[32] Schlumberger Information Systems, Eclipse Technical Description, 2002.
[33] Norsk Hydro Research Center, FIRST Reference Manual, Internal Technical Report, 2001.
[34] S.H. Lee, H. Tchelepski, L.F. De Chant, Implementation of a flux-continuous finite difference method for stratigraphic, hexahedron grids, in: Proceedings of the 1999 SPE Reservoir Simulation Symposium, Houston, TX, SPE 51901.
[35] W. Hackbusch, Theorie und Numerik elliptischer Differentialgleichungen, Teubner, Stuttgart, 1986, English Transl. (Springer, Berlin, 1992).
[36] M.H. Protter, H.F. Weinberger, Maximum Principles in Differential Equations, Springer, New York, 1984.
[37] A. Berman, R.J. Plemmons, Nonnegative Matrices in the Mathematical Sciences, Academic Press, New York, 1979.
[38] T.F. Russell, Relationships among some conservative discretization methods, Lecture Notes in Physics (1999) 1–16.
[39] R.A. Klausen, T.F. Russell, Relationships among some locally conservative discretization methods which handle discontinuous coefficients. Comput. Geosci. (to appear).
[40] D.K. Ponting, Corner point geometry in reservoir simulation, in: P.R. King (Ed.), Proceedings of the 1st European Conference on the Mathematics of Oil Recovery, Cambridge, 1989, Clarendon Press, Oxford, 1992, pp. 45–65.